



Time-domain Study of the Young Massive Cluster Westerlund 2 with the *Hubble Space Telescope*. I

E. Sabbi¹, M. Gennaro¹, J. Anderson¹, V. Bajaj¹, N. Bastian², J. S. Gallagher, III³, M. Gieles⁴, D. J. Lennon^{5,6}, A. Nota^{1,7}, K. C. Sahu¹, and P. Zeidler^{1,8}

¹ Space Telescope Science Institute, 3700 San Martin Drive, Baltimore, MD 21218, USA; sabbi@stsci.edu

² Astrophysics Research Institute, Liverpool John Moores University, 146 Brownlow Hill, Liverpool L3 5RF, UK

³ Department of Astronomy, University of Wisconsin-Madison, 5534 Sterling, 475 North Charter Street, Madison, WI 53706, USA

⁴ Department of Physics, University of Surrey, Guildford GU2 7XH, UK

⁵ Instituto de Astrofísica de Canarias, E-38200 La Laguna, Tenerife, Spain

⁶ Departamento de Astrofísica, Universidad de La Laguna, E-38205 La Laguna, Tenerife, Spain

⁷ ESA, SRE Operations Division, Spain

⁸ Department of Physics and Astronomy, Johns Hopkins University, Baltimore, MD 21218, USA

Received 2018 May 18; revised 2020 January 14; accepted 2020 February 5; published 2020 March 18

Abstract

Time-domain studies of pre-main-sequence (PMS) stars have long been used to investigate star properties during their early evolutionary phases and to trace the evolution of circumstellar environments. Historically these studies have been confined to the nearest, low-density, star-forming regions. We used the Wide Field Camera 3 on board the *Hubble Space Telescope* to extend, for the first time, the study of PMS variability to one of the few young massive clusters in the Milky Way, Westerlund 2. Our analysis reveals that at least one-third of the intermediate- and low-mass PMS stars in Westerlund 2 are variable. Based on the characteristics of their light curves, we classified $\sim 11\%$ of the variable stars as weak-line T Tauri candidates, $\sim 52\%$ as classical T Tauri candidates, $\sim 5\%$ as dippers, and $\sim 26\%$ as bursters. In addition, we found that 2% of the stars below $6 M_{\odot}$ ($\sim 6\%$ of the variables) are eclipsing binaries, with orbital periods shorter than 80 days. The spatial distribution of the different populations of variable PMS stars suggests that stellar feedback and UV radiation from massive stars play an important role in the evolution of circumstellar and planetary disks.

Unified Astronomy Thesaurus concepts: Pre-main sequence stars (1290); Star formation (1569); Star forming regions (1565); T Tauri stars (1681); Weak-line T Tauri stars (1795); Eclipsing binary stars (444); Variable stars (1761); Young star clusters (1833)

1. Introduction

Pre-main-sequence (PMS) stars have long been known to be variable objects (Joy 1945). Over the past 50 yr, studies of their variability have been used, for example, to characterize how stars accrete mass from their circumstellar disks (i.e., Hartmann et al. 1993; Bell & Lin 1994; D’Angelo & Spruit 2010; Cody et al. 2017), estimate PMS star rotational velocities (Hartmann & Stauffer 1989; Marilli et al. 2007; Venuti et al. 2017, i.e.), infer properties of the circumstellar disks, and trace the evolution of the circumstellar environment (e.g., Hillenbrand et al. 2002).

Young star clusters are excellent laboratories to study the evolution of PMS stars and their circumstellar disks, as they provide rich samples of objects having approximately the same age, distance, and chemical composition over a wide range of masses. These systems are characterized by large dust extinction, bright background level, and high stellar crowding. Therefore the study of PMS star time series have been, so far, limited to the closer and/or lower stellar density star-forming regions, such as the Orion Nebula Cluster (e.g., Stassun et al. 1999; Herbst et al. 2002; Stassun et al. 2007; Rice et al. 2015), NGC 1893 (Lata et al. 2012), ρ Oph and Upper Sco (Cody et al. 2017), NGC 2264 (Alencar et al. 2010; Cody et al. 2017; Cody & Hillenbrand 2018), and Stock 8 (Lata et al. 2019), thus covering only a limited range of parameters in terms of star formation rate, stellar density, and feedback.

The exquisite sensitivity and spatial resolution of the *Hubble Space Telescope* (*HST*) allow us to extend time-domain studies to the population of PMS stars in young clusters (age < 5 Myr)

more massive than $10^4 M_{\odot}$ (a.k.a. young massive clusters, YMCs). These systems trace intense episodes of star formation (SF), and because they are bright, can be observed at several tens of megaparsecs from us, in interacting and starburst galaxies.

In the Milky Way (MW) and in the Local Group (LG) YMCs are rare. Yet these few examples, close enough to be resolved into stars, are of prime interest for studying the formation and evolution of stars over more than three orders of magnitude (from over $100 M_{\odot}$ down to the hydrogen burning limit $\sim 0.1 M_{\odot}$) in regions characterized by extreme stellar densities and UV radiation. Time-series analyses of nearby YMCs, thus, offer the unique opportunity to collect rich samples of variable stars over a wide range of masses to characterize the earlier phases of PMS star evolution, mass accretion rates, and circumstellar disk survivability in environments that, in many ways, resemble the extreme conditions found in more distant interacting and starburst galaxies, in the early phases of globular cluster formation and in the early universe.

In this paper we present the first *HST* time-domain study of the galactic YMC Westerlund 2 (Wd2; Westerlund 1961). With an age of 1 to 2 Myr (Vargas Álvarez et al. 2013; Zeidler et al. 2015) and a stellar mass of $M = 3.6 \times 10^4 M_{\odot}$ (Zeidler et al. 2017), Wd2 is one of the most massive YMCs in the MW. The cluster is located in the Sagittarius spiral arm, at $\simeq 4.16$ kpc from the Sun (Vargas Álvarez et al. 2013; Zeidler et al. 2015). It hosts a rich population of OB-type stars (Moffat et al. 1991; Vargas Álvarez et al. 2013), including a double-line binary WR-star

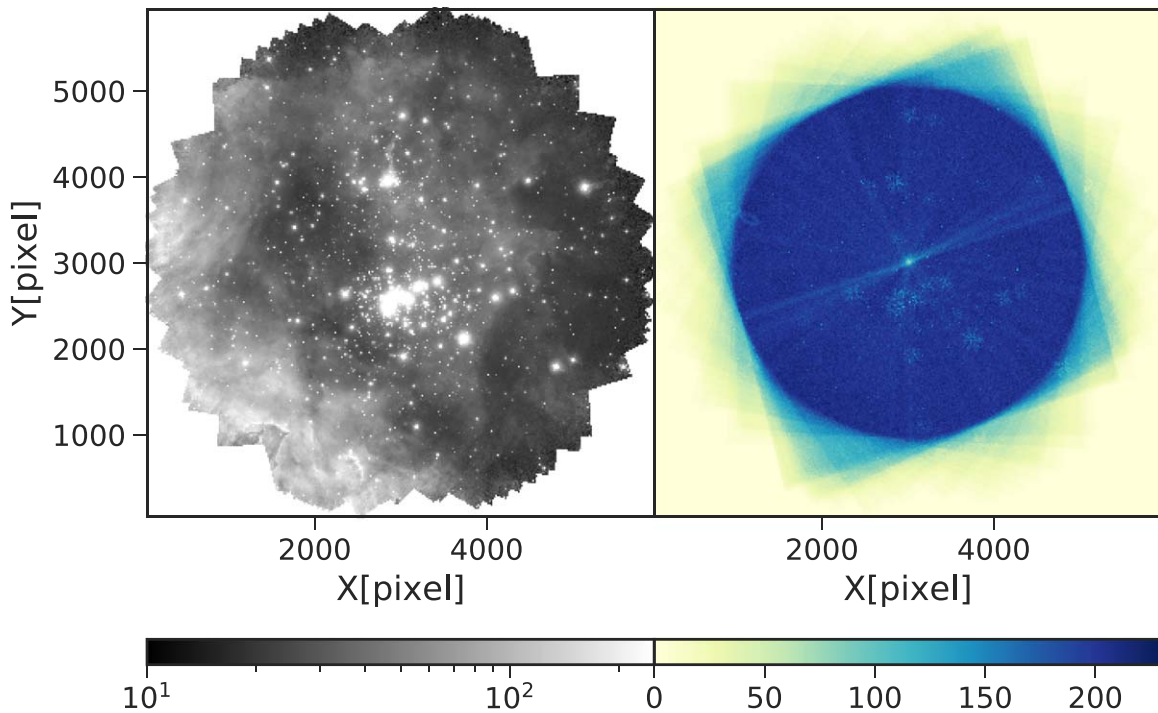


Figure 1. Left panel—stack image of Wd2, obtained combining all the deep exposures acquired in the UVIS filter F814W. North is up and east is to the left. The pixel scale is 40 mas/pixels. At the distance of Wd2 (Zeidler et al. 2015, 4.16 kpc) this translates to 0.02 pc/pixels. Right panel—coverage map of Wd2 mosaic. The darker the image, the greater the number of overlapping exposures.

with component minimum masses of $83.0 \pm 5.0 M_{\odot}$ and $82.0 \pm 5.0 M_{\odot}$ respectively (Bonanos et al. 2004).

Using the *HST* Advanced Camera for Surveys (ACS; filters F555W, F658N, and F814W) and the Wide Field Camera (WFC3) IR channel (filters F125W, F128N, and F160W, PI Nota, GO-13038) we found that the cluster consists of two nearly coeval clumps (Zeidler et al. 2015), and that is mass segregated (Zeidler et al. 2017). Following the same approach described in De Marchi et al. (2010), we identified a rich population of PMS stars with $H\alpha$ excess, that are likely still accreting material from their circumstellar disks (Zeidler et al. 2016)

The paper is organized as follows. In Section 2 we present the data and describe how we created the reference frame and performed the photometric reduction. We discuss the characteristics of the color–magnitude diagrams (CMDs) in Section 3 and the selection criteria used to identify the variable stars in Section 4. We classify the variable stars and describe their properties in Section 5. Conclusions are presented in Section 6.

2. Observations and Data Reduction

2.1. The Data

We repeatedly observed the YMC Wd2 from 2016 to 2019 October for a total of 47 orbits of *HST*, using the UVIS channel of WFC3 (PI Sabbi, GOs-14087, 15362, and 15514). Each orbit consists of two 3 s (hereafter short exposures) and six 350 s (hereafter long exposures) observations in the filter F814W. For the long exposures, we adopted a six-point dither pattern with a step of $1''.26$ to guarantee an optimal sampling of the point-spread function (PSF), fill the gap between the UVIS detectors, and allow for hot pixel removal. The two short exposures were acquired at the beginning and at the end of each orbit, respectively, at the same position of the first and last long

exposures. To identify and characterize the various types of Wd2 variable stars (periodic, semiperiodic, and nonperiodic), we organized the observations in groups of 5 or 10 visits using a nonuniform, logarithmic increasing spacing.

In this paper we limit our analysis to the long exposures, acquired during the first 26 visits, taken between 2016 October 30th and 2018 July 5th. Over this period we collected a total of 156 long exposures organized as follows:

1. The first five epochs were separated by 51 days each, and were acquired between 2017 October and June.
2. In 2017 August we observed Wd2 10 times with a 0.8 day cadence.
3. And 1.6 days later we obtained the other five epochs, each separated by 1.6 days.
4. The first epoch belonging to the 102 days cadence was observed on 2017 November 27th.
5. Lastly, five epochs separated by 3.2 days were acquired between 2018 March 9th and July 5th.

In Zeidler et al. (2015) we showed that Wd2 consists of two nearly coeval clumps. To guarantee the best coverage of the entire cluster population, we centered the gap among the two UVIS CCDs between the two clumps, in a region almost devoid of stars. To allow for a more flexible scheduling of the observations, we did not request any specific orientation. The left panel of Figure 1 shows the stack image, obtained by combining all deep exposures, while the right panel shows the coverage map of the survey, and highlights how many images contributed to each pixel.

2.2. The Reference Catalog

We carried out the photometric analysis directly on the bias-subtracted, flat-fielded, and charge-transfer-efficiency corrected `_flc.fits` exposures produced by the standard calibration

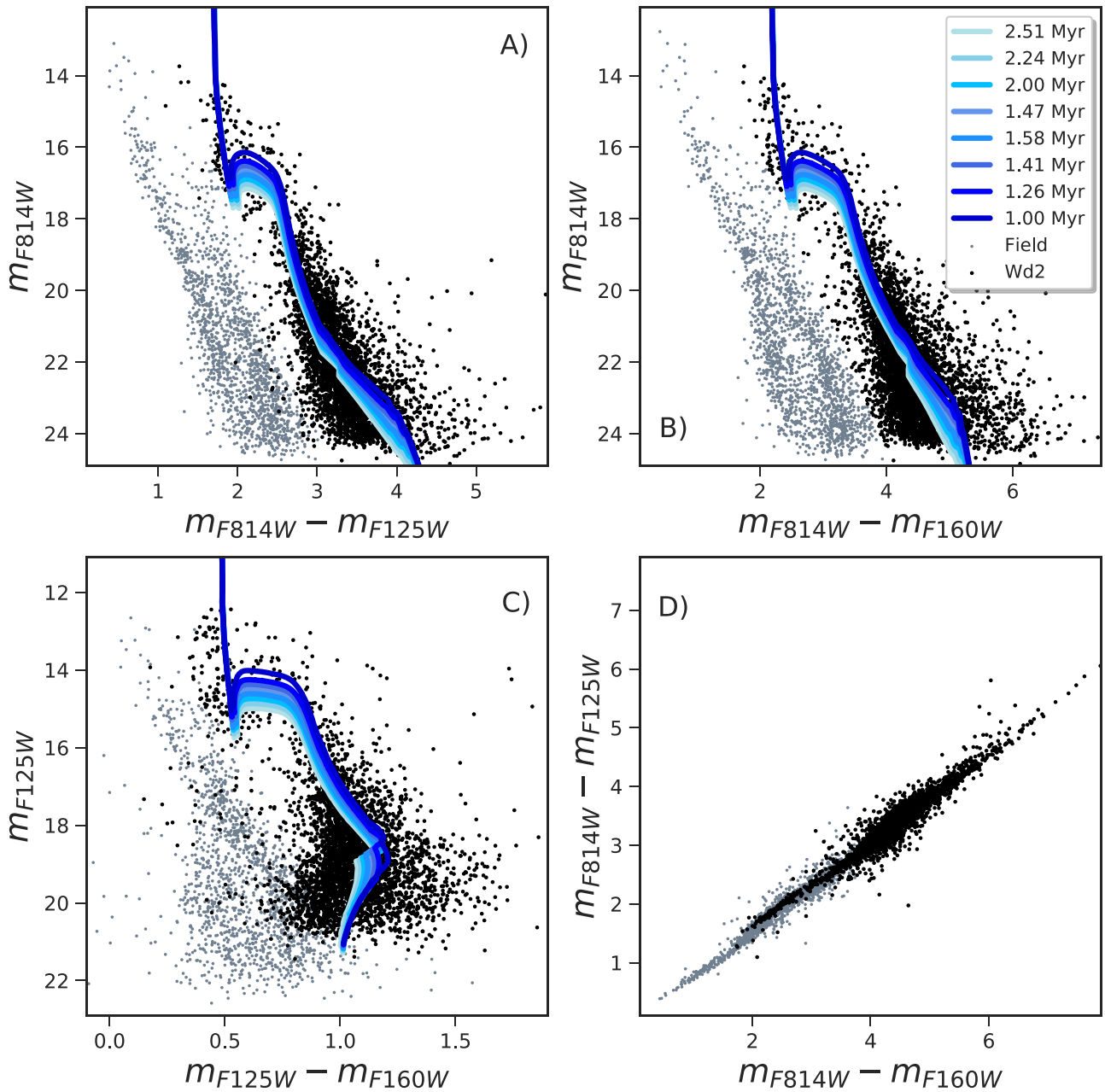


Figure 2. Wd2 color-magnitude diagrams for the filter combinations m_{F814W} vs. $m_{F814W} - m_{F125W}$ (panel (A)), m_{F814W} vs. $m_{F814W} - m_{F160W}$ (panel (B)), and m_{F125W} vs. $m_{F125W} - m_{F160W}$ (panel (C)). Panel (D) shows the color-color diagram $m_{F814W} - m_{F125W}$ vs. $m_{F814W} - m_{F160W}$. Cluster candidates are shown as black dots, while gray points are used for the stars in the field of the MW. Padova isochrones for solar metallicity and ages between 1.0 and 2.5 Myr are plotted over the cluster stellar population for reference, by assuming the distance of 4.16 kpc and the average extinction $R_v = 3.8$, that we derived in Zeidler et al. (2015).

pipeline calwf3 v3.5.⁹ Compared to drizzled (`_drc`) images, `_flc` images have the advantage of not being resampled and therefore they are the most direct representation of the astronomical scene. However `_flc` images are still affected by geometric distortion, which we took into account by creating a distortion-free reference frame and relating the photometry and astrometry of each exposure to that frame.

We used the publicly available one-pass photometry routine `img2xym` (Anderson & King 2006) and a library of empirical PSFs to identify and measure all the high signal-to-noise ratio

($S/N > 150$), isolated (within 5 pixel radius), and nonsaturated sources. The PSF library properly accounts for the spatial variations caused by the optics of the telescope and the variable charge diffusion in the CCD. Seasonal and daily thermal changes, however, can cause variations in the optical path length of *HST* up to a few microns within the timescales of an orbit (Bély et al. 1993; Lallo et al. 2006). These changes affect the focus of the telescope and translate to small, but measurable differences in the PSF from one exposure to another. To take these variations into account, for each exposure we derived the correction necessary to minimize its average PSF-residuals. We then derived for each catalog a six-parameter transformation to align the UVIS observations to the

⁹ Gennaro, M., et al. 2018, “WFC3 Data Handbook,” version 4.0 http://www.stsci.edu/hst/wfc3/documents/handbooks/currentDHB/wfc3_dhb.pdf.

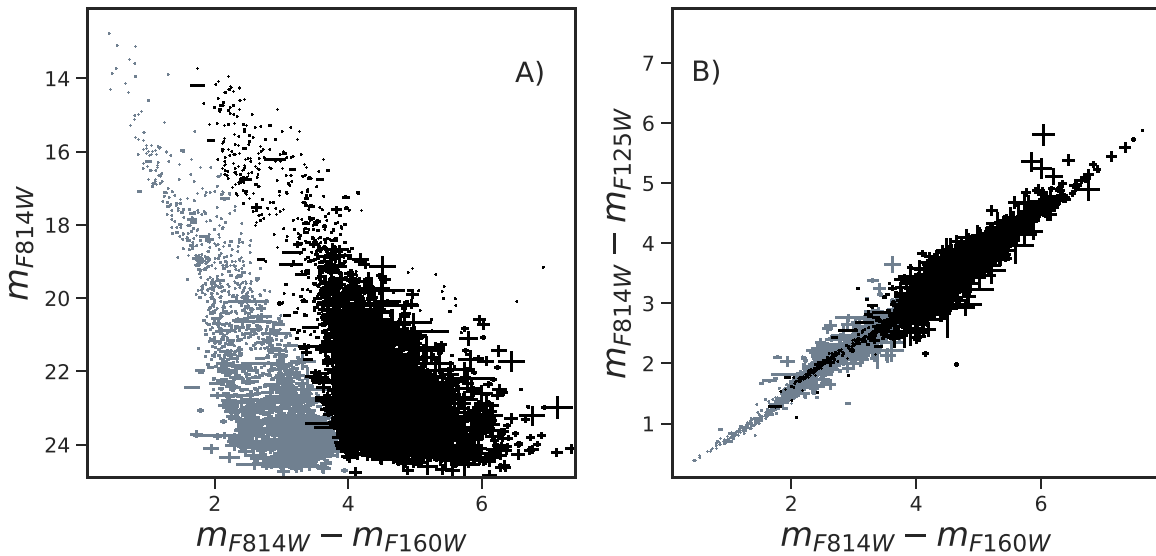


Figure 3. Panel (A) CMD m_{F814} vs. $m_{F814W} - m_{F160W}$. The size of the symbols represents the photometric errors. Panel (D) The color-color diagram $m_{F814} - m_{F160W}$ vs. $m_{F814W} - m_{F125W}$. As in panel (A) the symbol size measures the photometric error.

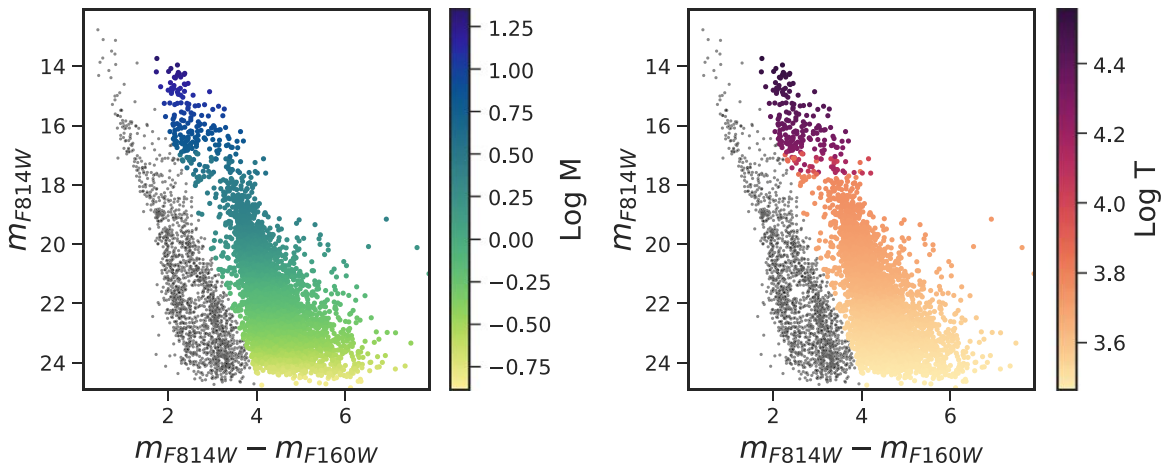


Figure 4. CMD of Wd2 for the filter combination m_{F814} vs. $m_{F814W} - m_{F160W}$. In the left panel cluster stars are color-coded based on their mass, and in the right panel Wd2 stars are color-coded based on their temperature. Temperatures and masses were derived using the 1.6 Myr old Padova isochrones for solar metallicity, assuming a distance of 4.16 kpc and average extinction $R_v = 3.8$. In both cases we used a logarithmic scale. MW field stars are shown as black dots.

Gaia Data Release 2 (DR2, Lindegren et al. 2018), and to create a distortion-free reference frame with a pixel scale of 40 mas/pixel, the UVIS native pixel scale.

To separate candidate members of Wd2 from the field of the MW, and to estimate masses and temperatures of the stars in the cluster, we combined our data with our previous WFC3/IR observations acquired in the filters F125W and F160W (PI Nota, GO-13038). We aligned the IR observations to *Gaia* using the same procedure followed for UVIS.

The final photometric analysis was performed using the software KS2 (J. Anderson 2020, in preparation; see Sabbi et al. 2013, 2016, for details), that can use all the exposures together to detect, measure, and subtract stars in subsequent passes, moving from the brightest to the fainter sources. KS2 can perform simultaneous detection in multiple filters. However, given the higher spatial resolution of the UVIS data set, we only used the long exposures acquired through the UVIS/F814W filter to create the reference catalogs. For each source KS2 provides the mean flux, the flux standard deviation, and an estimate of the quality of the fit of the PSF. The final catalog contains in total 9268 sources.

The fluxes of the sources found by KS2 in the UVIS/F814W combined observations were measured in the WFC3/IR exposures, and in each of the individual F814W visits. For each exposure we used its own “focus-specific” PSF library, derived as described above.

Fluxes were converted into instrumental magnitudes and then calibrated in the Vega-mag photometric system following the same approach described in Sabbi et al. (2016), and using the zero-points listed on the STScI website.¹⁰ The aperture correction was derived using a $0''.4$ aperture photometry on the drizzled images.

3. The Color-Magnitude Diagrams

Figure 2 shows Wd2 CMDs and the color-color diagram in the combination of filters:

$$\begin{aligned} & m_{F814} \text{ versus } m_{F814W} - m_{F125W}, \\ & m_{F814} \text{ versus } m_{F814W} - m_{F160W}, \end{aligned}$$

¹⁰ <http://www.stsci.edu/hst/instrumentation/wfc3/data-analysis/photometric-calibration/uv-vis-photometric-calibration>

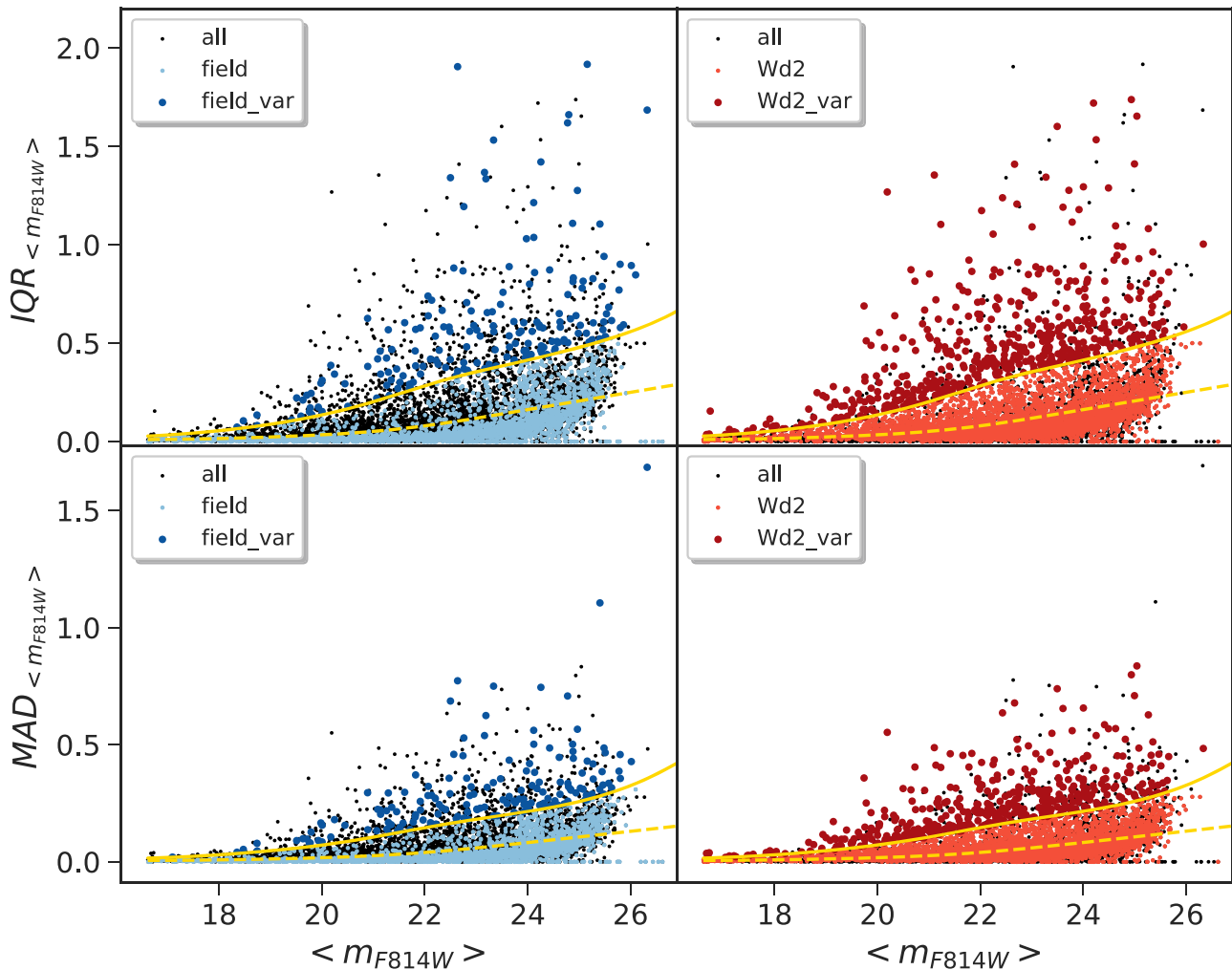


Figure 5. Upper panels: distribution of the IQR value as a function of magnitude for the stars that have been observed in at least 16 visits. Field stars are shown in the left panel in blue and Wd2 candidates are shown in red in the right panel. The yellow dashed line marks the running mean of the entire population, the continuous yellow line is $1.349 \times \sigma_{\text{IQR}}$. Lower panels: same as the upper panels but for the MAD statistics. The continuous yellow line represents $1.4826 \times \sigma_{\text{MAD}}$.

m_{F814} versus $m_{\text{F814W}} - m_{\text{F125W}}$ shows the color-color diagram $m_{\text{F814}} - m_{\text{F160W}}$ versus $m_{\text{F814W}} - m_{\text{F125W}}$.

From now on in each plot we show mean magnitudes and colors as derived from the combination of all the single exposures.

In all three CMDs shown in Figure 2 it is possible to identify two well separated populations, with the bluer sequence belonging to the field of the MW. Wd2 intermediate and high-mass main-sequence (MS) stars ($m_{\text{F814W}} \leq 15.7$) and low-mass PMS stars ($m_{\text{F814W}} \geq 17.5$) stars occupy the redder sequence. The Turn On (TO_n), the point where the PMS stars arrive in MSs, is well defined between $15.7 < m_{\text{F814W}} < 17.5$.

We defined as candidate members of Wd2 the 6133 sources whose mean magnitudes met the selection criteria $6.7 \times (m_{\text{F814W}} - m_{\text{F160W}}) - 1.59 \times (m_{\text{F814W}} - 17.1) > 0$. In all four plots of Figure 2, cluster candidates are shown as black dots, while field stars are in gray. Padova isochrones (Marigo et al. 2017; Pastorelli et al. 2019) for solar metallicity and in the age range between 1.0 and 2.5 Myr are shown for reference, assuming the same distance $D = 4.16$ kpc and average extinction $R_v = 3.8$, that we derived in Zeidler et al. (2015).

In the F814W filter the photometric errors, determined using the formula $\sigma_{\text{mag}} = 1.1 \sigma_{\text{flux}} / \text{flux}$, range from 0.001 to 0.787, and in the filter F160W from 0.001 to 0.866. The effect of the photometric errors at the various magnitudes and colors of the m_{F814} versus $m_{\text{F814W}} - m_{\text{F160W}}$ CMD are shown in panel (A) of Figure 3. Down to magnitude $m_{\text{F814W}} \simeq 23$ the photometric errors are small enough to not affect the separation between cluster and MW field. The effect of the photometric errors in the color-color diagram are shown in panel (B) of the figure.

We used the 1.58 Myr isochrone to infer an estimate of the masses and temperatures of the sources that likely belong to the Wd2 cluster, and we found that in our observations we cover the mass range between 0.1 and $22.7 M_{\odot}$ and temperatures between 3000 and 36,000 K. We emphasize that these values are highly model dependent, and should be taken only as an indication of the properties of the stellar population, and not as the definitive value of a specific source. The distribution of masses and temperature in the m_{F814} versus $m_{\text{F814W}} - m_{\text{F160W}}$ CMD is shown in Figure 4 using a logarithmic scale. In this paper we limit our analysis to the 4950 sources fainter than $m_{\text{F814W}} \lesssim 16.62$ that likely belong to the Wd2 population. Using Padova isochrones, this corresponds to the mass range between $0.1 \lesssim M \lesssim 5.8 M_{\odot}$.

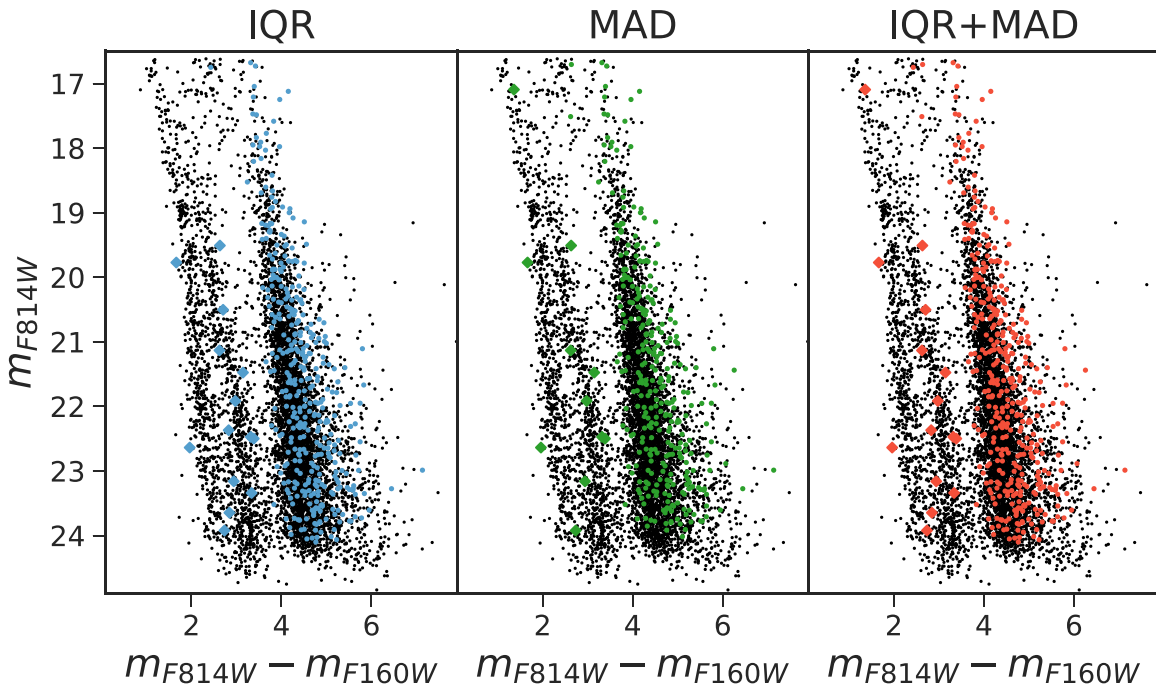


Figure 6. Colors and magnitudes of the variable stars as detected using the IQR statistics (shown as blue points in the left panel, the MAD statistics (shown as green points in the middle panel) and a combination of both (red points in the right panel).

4. Variability Search

The right panel of Figure 1 shows that the innermost 80'' from the center of the image are uniformly covered by the observations, while between 80'' and 114'' the number of exposures per pixel is considerably variable. To guarantee sufficient statistics, we limited the search for variability to those sources that were observed in at least 16 different visits.

To separate true variable sources from artifacts caused by cosmetic defects of the UVIS CCDs, diffraction spikes from saturated neighbors, and cosmic ray hits, we used two variability indices: the median absolute deviation (MAD, Rousseeuw & Croux 1993; Richards et al. 2011), and the interquartile range (IQR, Kim et al. 2014).

The MAD index measures the scatter of observations m_i and is defined as $\text{MAD} = \text{median}(|m_i - \text{median}(m_i)|)$. The MAD statistic is largely used because it is insensitive to outliers (Zhang et al. 2016); however, this makes it also insensitive to real occasional variations, such as the Algol-type eclipses (Sokolovsky et al. 2017). The IQR index is defined as the difference between the median values computed for the upper and lower halves of a data set, and it is preferable to MAD when dealing with an asymmetric distribution, and to detect the signal coming from eclipsing binaries.

PMS stars are known to be variable sources (Joy 1945). On the contrary we do not expect to find a high number of variable stars in the field of the MW, mainly populated by MS stars. Figure 5 shows the IQR (upper panels) and MAD (lower panels) statistics for our entire sample as a function of magnitude. The dashed yellow lines represent the mean of the distributions, while the continuous yellow lines mark the $1.349 \times \sigma_{\text{IQR}}$, and $1.4826 \times \sigma_{\text{MAD}}$ values respectively. MW stars are shown in blue in the left panels, with variable candidates marked with larger dark blue dots. Similarly, Wd2

stars are shown in orange in the right panels, and Wd2 variable candidates are shown as larger dark red dots. The corresponding position of the variable stars on the m_{F814W} versus $m_{\text{F814W}} - m_{\text{F160W}}$ CMD is shown in Figure 6.

5. Variable Classification

At least 30% (1473) of Wd2 stars between $0.1 \lesssim M \lesssim 5.8 M_{\odot}$ are variable, with peak-to-peak magnitude variations in the F814W filter ranging from 0.035 to 3.224 mag. We divided our sample in variables with peak-to-peak variations Δm_{F814W} below and above 0.75 mag. We used the Lomb–Scargle (Lomb 1976; Scargle 1982) periodogram, a well-known algorithm for detecting and characterizing periodic signals in unevenly sampled data, to find for each source its most plausible period (if any), and then to phase-fold its light curve (LC).

We inspected each LC by eye and divided our sample into five groups:

1. periodic sources with $\Delta m_{\text{F814W}} \leq 0.75$ were classified as weak-line T Tauri star (WTTS) candidates (these sources are further described in Section 5.1);
2. nonperiodic sources with $\Delta m_{\text{F814W}} \leq 0.75$ were classified as classical T Tauri star (CTTS) candidates (see Section 5.2 for more details);
3. nonperiodic sources that showed a decrease in magnitude $\Delta m_{\text{F814W}} \geq 0.75$ were classified as dippers (these sources are discussed in Section 5.3);
4. nonperiodic sources that showed outbursts in magnitude $\Delta m_{\text{F814W}} \geq 0.75$ were classified as bursters (the characteristics of bursters are presented in Section 5.4);
5. periodic sources with $\Delta m_{\text{F814W}} \leq 0.75$ were classified as eclipsing binary (EB) candidates (further discussion about EBs is presented in Section 5.5).

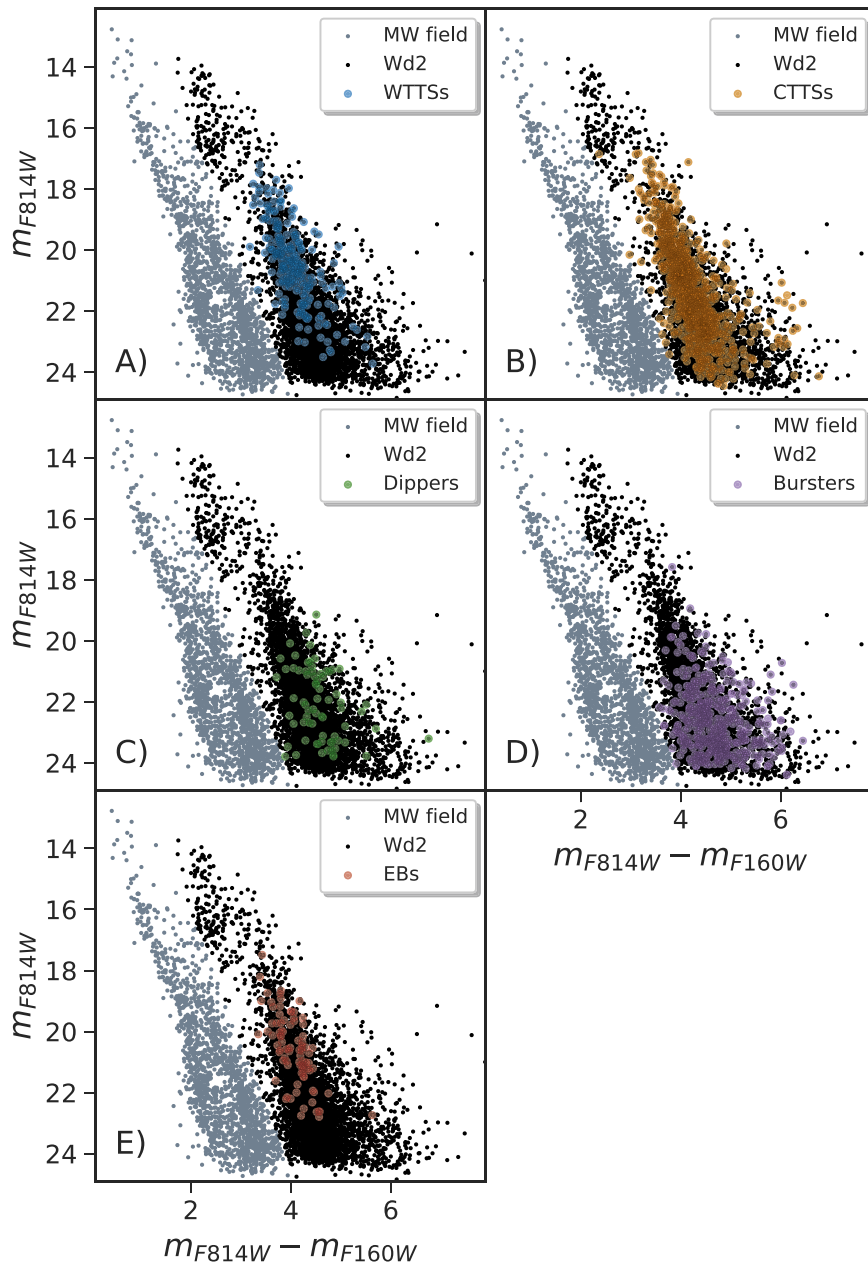


Figure 7. Colors and magnitudes of the five types of variable stars. WTTs candidates are shown in blue in panel (A). CTTS candidates are shown in orange in panel (B). Panel (C) shows colors and magnitudes of dipper candidates as green points, while burster candidates are shown in panel (D) as purple points. Candidates eclipsing binaries are shown in panel (E) in red.

5.1. WTTs Candidates

The LCs of WTTs are thought to be dominated by the asymmetric distribution of cool or dark magnetic spots on the stellar surface, with stellar rotation being responsible for the modulation of the fluxes (Bouvier et al. 1993; Herbst et al. 1994). These sources show minimal to no evidence of ongoing accretion, possibly because the innermost part of their circumstellar disks have already been depleted.

Three percent of Wd2 stars fainter than $m_{F814W} = 17.0$ show periodic (with periods ranging between 1.6 and 46 days, and with an average value of 7.7 days), small-amplitude ($0.035 \times \Delta m_{F814W} \leq 0.75$ mag) fluctuations consistent with Class III WTTs. The position of the WTTs candidates in the m_{F814W}

versus $m_{F814W} - m_{F160W}$ CMD is shown in panel (A) of Figure 7. The number of WTTs candidates considerably decreases below $m_{F814W} \simeq 21.5$, with the faintest source found at $m_{F814W} \lesssim 23.8$. This drop is likely caused by incompleteness effects. In a future paper, we will examine all the 47 orbits of *HST* time and perform artificial star tests to evaluate the impact of various selection biases, including temporal sampling, S/N, and crowding, on the five populations of variables. Panel (A) in Figure 8 shows that the WTTs candidates have relatively blue colors, in agreement with the hypothesis that these objects are likely quite evolved PMS stars.

We used the Stefan–Boltzmann law to convert the luminosities and temperatures derived from Padova isochrones into stellar radii ($1.5 \leq R_{WTTs} \leq 5.7R_{\odot}$). In doing this we

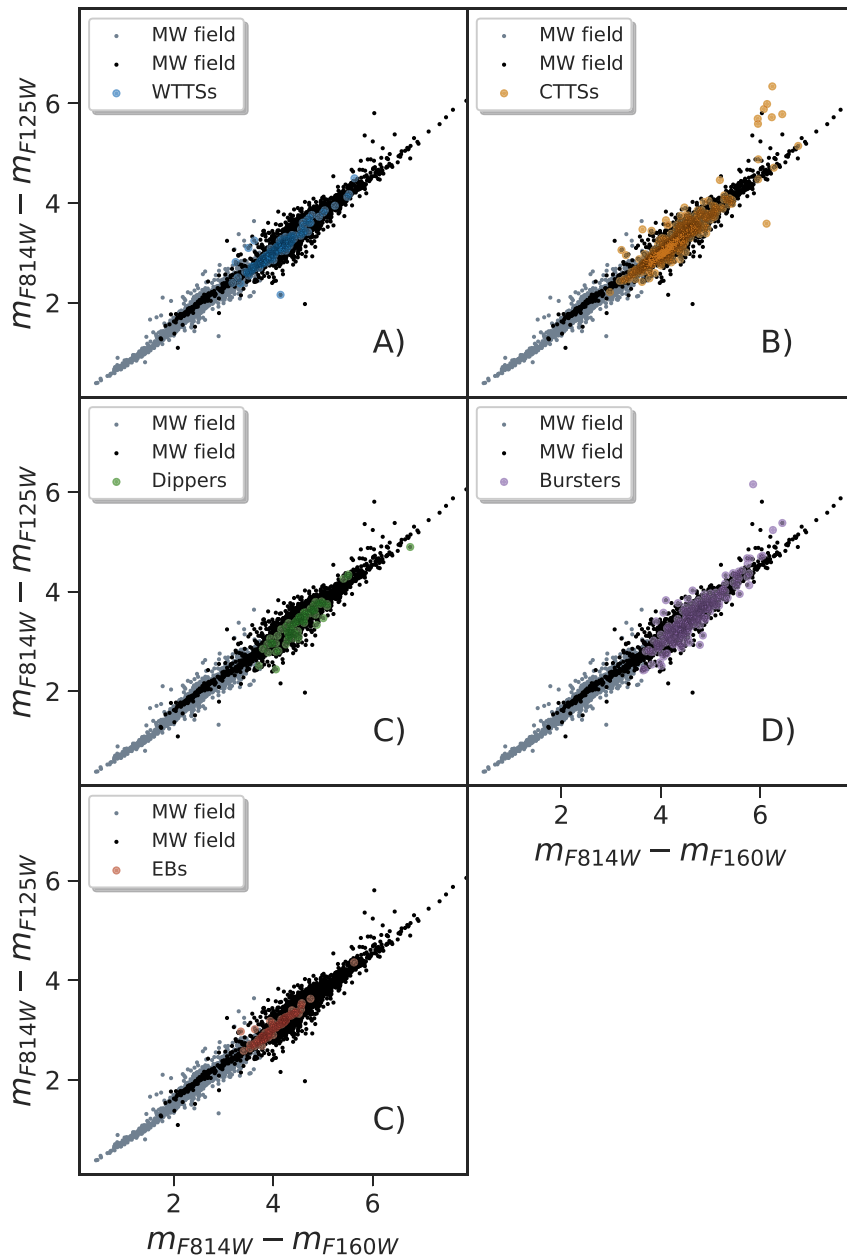


Figure 8. Wd2 color-color diagram with the five classes of variables superimposed using the same color-scheme adopted in Figure 7.

found that the rotational velocities $v \sin(i)$ of the WTTs candidates range between 2.3 and $\sim 168 \text{ km s}^{-1}$, with a peak at $\sim 12.5 \text{ km s}^{-1}$, in agreement with the $v \sin(i)$ measurements found in the literature (i.e., Clarke & Bouvier 2000; Herbst et al. 2002; Xing et al. 2006).

5.2. CTTs Candidates

CTTs are class II young stellar objects that are still actively accreting material from their circumstellar disks. We identified 757 variable sources ($\sim 15\%$ of Wd2 low-mass stars) whose LCs are highly variable, but do not show evidence for periodicity on a short timescale. These objects cover the magnitude range $17.0 \lesssim m_{F814W} \lesssim 24.2$ (panel (B) of Figure 7), and, compared to WTTs candidates, extend toward redder colors both in $m_{F814W} - m_{F125W}$ and in $m_{F814W} - m_{F160W}$ (Figure 8).

5.3. Dipper Candidates

A special class of CTTs was discovered about 10 yr ago. These objects are characterized by largely flat LCs, interrupted by sharp and short dips, and they are therefore often referred to as “dippers” (Alencar et al. 2010; Morales-Calderón et al. 2011; Cody et al. 2014; Ansdell et al. 2016; Hedges et al. 2018). Because the dips are normally shallower in the IR than at optical wavelengths, they have been attributed to large and dusty structures (such planetesimals) passing along our line of sight (Bouvier et al. 2003; Alencar et al. 2010; McGinnis et al. 2015), although their precise location within the disk (inner versus outer disk, Bouvier et al. 1999; Morales-Calderón et al. 2011; Bodman et al. 2017) is still debated.

Seventy-two of the sources in Wd2 between $19.14 \leq m_{F814W} \leq 23.79$ ($0.3 \leq M \leq 2.4 M_{\odot}$) show relatively flat LCs, interrupted by sudden drops in luminosity as large as 2.78 mag

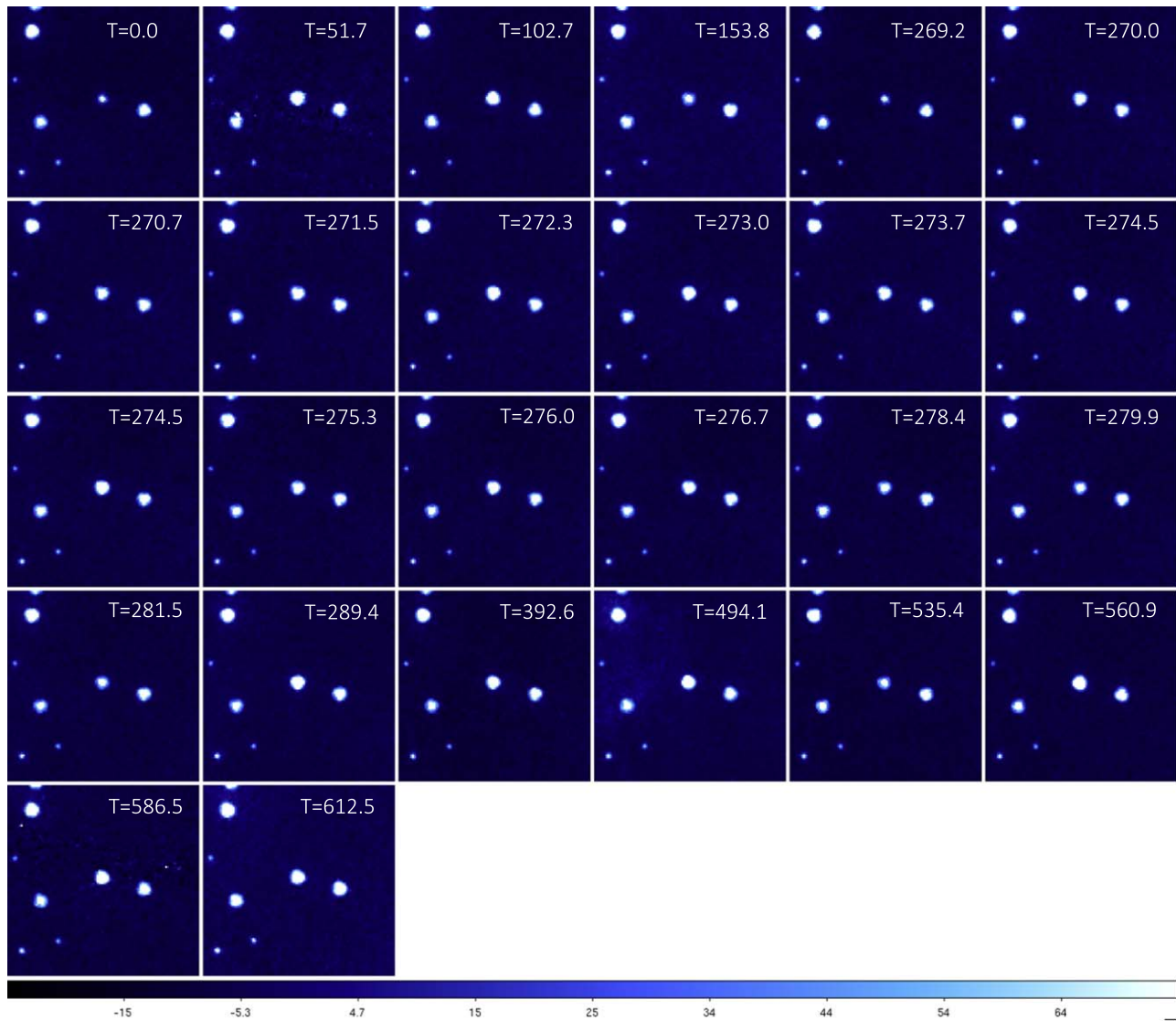


Figure 9. Images of star #5320 acquired between 2016 October and 2018 July in the filter F814W. North is up and east is left. On 2018 October 30th the star was at its minimum luminosity, corresponding to $m_{F814W} = 23.26$. In 51 days its magnitude rose to $m_{F814W} = 21.423$ and remained roughly constant for the next 100 days. One hundred days later the magnitude dropped again to $m_{F814W} = 23.16$. After that, the star maintained an average magnitude $m_{F814W} = 21.69 \pm 0.32$, with an average photometric error of 0.016. Time in days from the first observation is shown at the top of each image.

in the m_{F814W} filter. Based on our temporal coverage, we conclude that the observed drops in luminosity are short events, that last a few tens of days at most. An example of this type of object is shown in Figure 9, where the luminosity of the star #5320 (R.A. = $10^{\text{h}}24^{\text{m}}05^{\text{s}}.463$, decl. = $-57^{\circ}45'08''.838$, J2000) in the filter F814W dropped by ~ 2.0 mag two times in less than two years.

5.4. Bursters

In Wd2 about 8% of the stars fainter than $m_{F814W} \lesssim 16.62$ are characterized by eruptive behaviors, with the largest increase in magnitude we observed so far being $\Delta m_{F814W} = 3.22$. In some cases the variation lasts for only a few days, in others, once the star lights up, its luminosity remains elevated.

Eruptive low-mass PMS stars are common and, based on the length of their burst, have been classified as either EX Orionis-type (short burst Herbig 2007) or FU Orionis-type (few year long burst, Hartmann & Kenyon 1996; Hartmann et al. 1998)

stars. It is not clear yet if EXor- and FUor-type stars belong to the same class of objects, or if all the young low-mass stars undergo a bursting period. Nevertheless for both EXor- and FUor-type stars, the large variation in brightness is ascribed to unstable pile-up of gas in the inner disk, which then releases a cascade of material onto the star. It is believed that most of the stellar mass is accumulated via these dramatic outbursts (e.g., Bell & Lin 1994; Zhu et al. 2009; D’Angelo & Spruit 2010), during which a star can accrete up to $0.01M_{\odot}$ of gas.

WISE observations of “burster” stars, identified during the K2 mission, show clear IR excess, typical of large inner circumstellar disks, and the strength of the outburst appears to correlate to the IR excess (Cody et al. 2017). These bursts are likely “cooking” the dust in the circumstellar disks, and thus modifying their chemical composition (Green et al. 2006; Quanz et al. 2007; Cieza et al. 2016). Understanding the properties and the frequency of these bursting systems is therefore important for the models of stellar mass accretion,

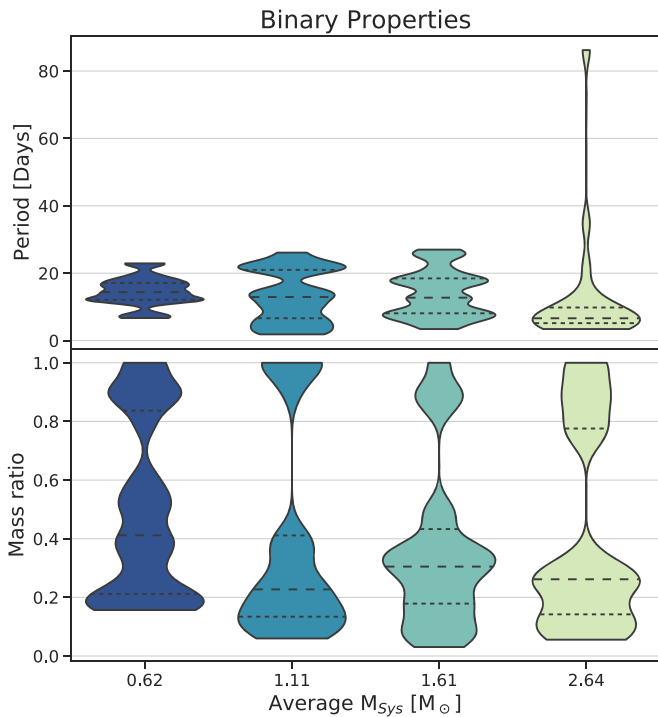


Figure 10. Violin plots for binary systems in four different mass bins. The upper panel shows the distribution of periods, expressed in days, while the lower panel shows the distribution of mass ratios Q . In both panels the dashed line marks the median value of the distribution, and the two dotted lines show the first and third quartile respectively. The width of each violin is scaled by the number of data in that bin.

protoplanetary gas-rich disk evolution, and, possibly, planet formation.

5.5. Eclipsing Binaries

The phase-folded LCs of nearly 2% of the objects between $0.1 \lesssim M \lesssim 5.8 M_{\odot}$ (panel (E) in Figure 7) show two minima, characteristic of eclipsing binaries. For each of these objects we derived physical and orbital properties by iteratively fitting their phase-folded LCs with the publicly available software *Nightfall*.¹¹

We assumed the orbital period and the ephemeris zero-point derived by the Lomb–Scargle statistics, and the total mass inferred from Padova isochrones. *Nightfall* then compared the observed LC with simulations obtained for different mass ratios, stellar temperatures, inclination angles, and Roche lobe filling factors using a chi-square function to determine the best-fit solution. The derived values depend on the assumptions made in modeling the stellar atmospheres in the *Nightfall* software and in the Padova isochrones, used to infer the total masses of the binaries. Therefore they should be used only for comparisons and not as absolute values. Because of the sparse cadence and the relatively short temporal coverage of our observations, in this preliminary study, we assumed only circular orbits, and, in the case of interacting binaries, in the LC model we did not include the contribution of a mass-transferring disk.

Because of the limited temporal sampling, our analysis is biased toward the shortest periods. Therefore we were able to find only eclipsing binaries with orbital periods ranging

between $1.9 \leq P \leq 86$ days, and separations between $6.8 \leq R \leq 108 R_{\odot}$ ($0.03\text{--}0.5$ au). The upper panel of Figure 10 shows the distribution of periods covered in four different bins of system masses. The lower panel shows the distribution of mass ratios ($Q = M_2/M_1$) for the same bins of mass. It is interesting to note that in all four bins the distribution of the Q parameter is bimodal, with only \sim one-third of the binaries consisting of nearly equal-mass objects, similar to what observed by Raghavan et al. (2010) for binary systems, with primary star having mass $M_1 \sim 1 M_{\odot}$.

In 50% of the systems the LCs are consistent with those of semidetached binaries where one of the two components (the primary in 40% of the cases and the secondary in the remaining 10%) has filled its Roche lobe. In 2% of the cases the LCs are consistent with those of contact binaries, with both stars having filled the Roche lobe. Because of the considerable fraction of interacting binaries, with ongoing mass transfer, it is likely that the mass ratio distribution will change over time, increasing the number of equal-mass systems. The distribution of the filling factors for both the primary (in red) and the secondary stars (in orange) for four different bins of masses is shown in Figure 11.

Figure 12 shows the mass to radius relation for the primary (blue circles) and the secondary (orange triangle) star as derived from the fitting of the EB LCs. The radii of the primary components range between $0.1 \leq R_p \leq 33.8 R_{\odot}$ and for the secondary between $0.1 \leq R_s \leq 13.6$. In many cases these values are considerably larger than those derived from Padova isochrones using the Stephan–Boltzmann law. Phenomena such as tidal heating, ohmic dissipation and thermal tides have been considered to explain the inflated radii observed in close binaries and hot Jupiters; however, in this case the fact that the library of models of atmosphere in *Nightfall* is not optimized to describe PMS stars and that the objects are quite far from the approximation of blackbodies is likely responsible for at least part of the discrepancies.

5.6. Distribution of the Variable PMS Stars

Figure 13 shows the spatial distribution of the five populations of variable PMS stars projected on an image of Wd2 taken through the filter F814W. Isodensity contours for the stars belonging to Wd2 are shown for reference in all five panels.

A visual inspection of Figure 13 suggests that WTTS candidates (panel (A)) are more concentrated around the two main clumps, while CTTS candidates (panel (B)) and bursters (panel (D)) extend toward larger radii. Given that WTTS candidates are relatively massive objects, this is likely only a consequence of the fact that Wd2 is mass segregated (Zeidler et al. 2015).

In relatively low-density star-forming regions, like NGC 2264, dippers represent about 20%–30% of the CTTS population (Alencar et al. 2010; Cody et al. 2017; Cody & Hillenbrand 2018) and from the analysis of *K2* mission data Hedges et al. (2018) found that dippers and bursters should have similar spatial distributions. However, panel (C) shows that in Wd2 dippers clearly avoid the two regions of highest density, where the majority of the high-mass stars (up to $80 M_{\odot}$ Bonanos et al. 2004) are concentrated. In particular, based on the number of bursters and CTTS found within 150 pixels (~ 1.12 pc) from the main clump of Wd2, in the same region we should find at least five dippers if they had the same spatial distribution of the other variable stars.

¹¹ Program and user manual can be downloaded from <https://www.hs.uni-hamburg.de/DE/Ins/Per/Wichmann/Nightfall.html>.

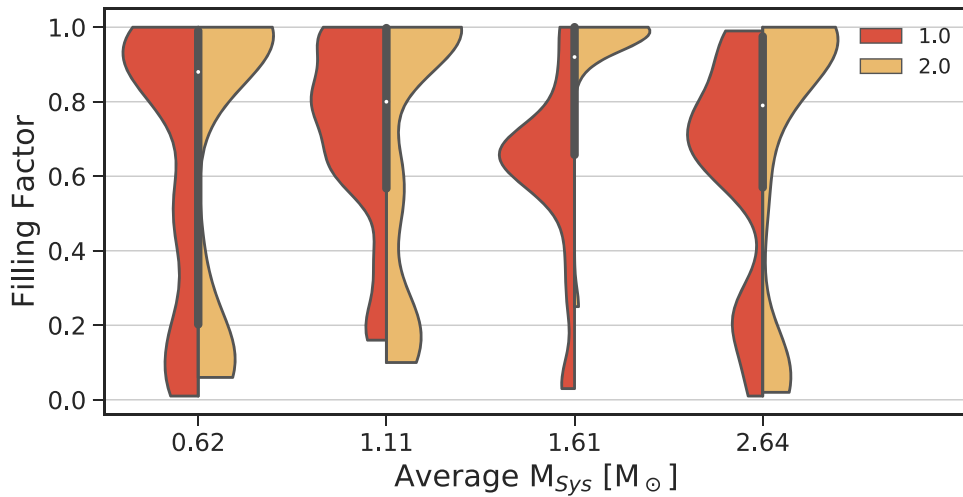


Figure 11. Distribution of the filling factors for the primary (in red) and secondary (in orange) star in four different bins of masses. When the filling factor is equal to unity, the star has filled its Roche lobe and is transferring mass to its companion.

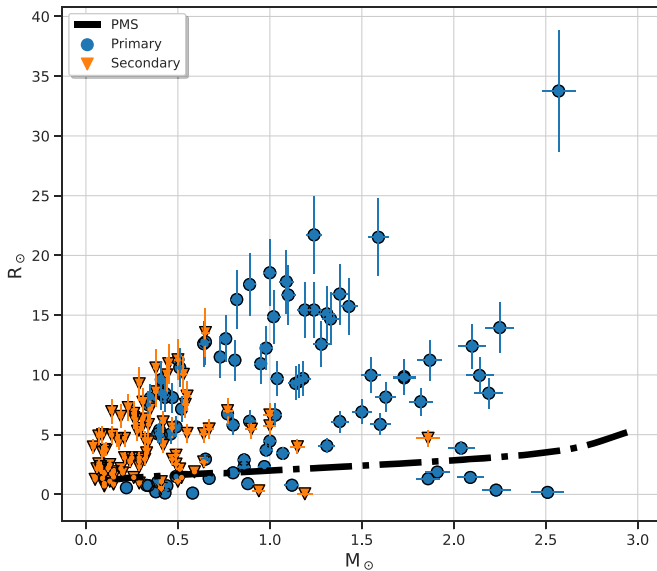


Figure 12. Mass to radius relation for both the primary stars (shown as blue circles) and the secondary (orange triangles) as derived by fitting the phase-folded LCs of the EBs. The dotted–dashed black line shows the mass to radius relation for 1.6 Myr old PMS stars of similar masses and metallicities as derived from Padova isochrones.

We used Ripley’s K function (Ripley 1977, 1979) to further investigate the clustering properties of the variable stars in Wd2. According to Ripley’s statistics, a population is considered clustered within a certain scale r if $K(r)$ is above the response of the K function for a Poisson distribution. On the contrary, distributions whose K function at the distance r are below the Poisson distribution are considered dispersed. Figure 14 compares the K functions for WTTS candidates (in blue), CTTS candidates (in orange), dippers (in green), bursters (in purple), and EBs (in red) to the K function of a Poisson distribution (black dashed line) over the entire range of magnitudes considered (panel (A)), for stars between $17 < m_{F814W} \leq 20.0$ (corresponding to the mass range between 1.75 and $3.3 M_{\odot}$ when using Padova isochrones, panel (B)), between $20 < m_{F814W} \leq 22.0$ (corresponding to the mass range between 0.8 and $1.8 M_{\odot}$, panel (C)), and between

$22 < m_{F814W} < 24.5$ (corresponding to the mass range between 0.2 and $0.8 M_{\odot}$, panel (D)).

Over the entire range of magnitudes ($17 < m_{F814W} < 24.5$, Figure 14 panel (A)) EBS, CTTS candidates, and bursters have the same clustering scale $r = 1.41 \pm 0.14$ pc and their K functions are indistinguishable from each other. On the same range of magnitudes, the clustering properties of WTTS candidates are less significant than those of the previous three populations, but their clustering scale is comparable ($r_{WTTS} = 1.32 \pm 0.14$ pc).

The clustering properties of the dippers between $17 < m_{F814W} < 24.5$ are only marginally significant, and in the innermost 0.08 ± 0.01 pc they are dispersed. Their clustering scale is also smaller than the other populations, being only $r_{Dip} = 1.05 \pm 0.20$ pc.

Because the cluster is mass segregated (Zeidler et al. 2017), we checked if Ripley’s statistics could give different results over different ranges of magnitude/masses. If we consider only the variable PMS stars brighter than $m_{F814W} \leq 20.0$, we find that EBs are significantly more clustered than CTTS and WTTS candidates. In this range of magnitudes CTTS and WTTS candidates have identical distributions, while bursters are almost indistinguishable from a Poisson distribution. Only four dippers are brighter than $m_{F814W} \leq 20.0$, and therefore we do not consider their distribution in this range of masses.

Between $20.0 < m_{F814W} \leq 22.0$, bursters have clustering properties and significance similar to CTTS candidates, while the properties of WTTS candidates resemble those of the EBs. On scales smaller than $r \simeq 800$ pixels (~ 0.7 pc) dippers’ properties are similar to those of EBs and WTTS candidates, but at larger scales they become more similar to bursters and CTTS candidates. Finally for magnitudes fainter than $m_{F814W} > 22.0$ only CTTS candidates and bursters are significantly clustered.

The lack of dippers in the regions of highest stellar density suggests that the properties of stellar disks vary with the position in the cluster, and that in less than 2 Myr phenomena such as dynamical truncation (Vincke et al. 2015; Portegies Zwart 2016; Vincke & Pfalzner 2016), stellar winds (Pelupessy & Portegies Zwart 2012), dynamical interaction (Olczak et al. 2008; Reche et al. 2009; de Juan Ovelar et al. 2012), and photoevaporation caused by the UV radiation coming from

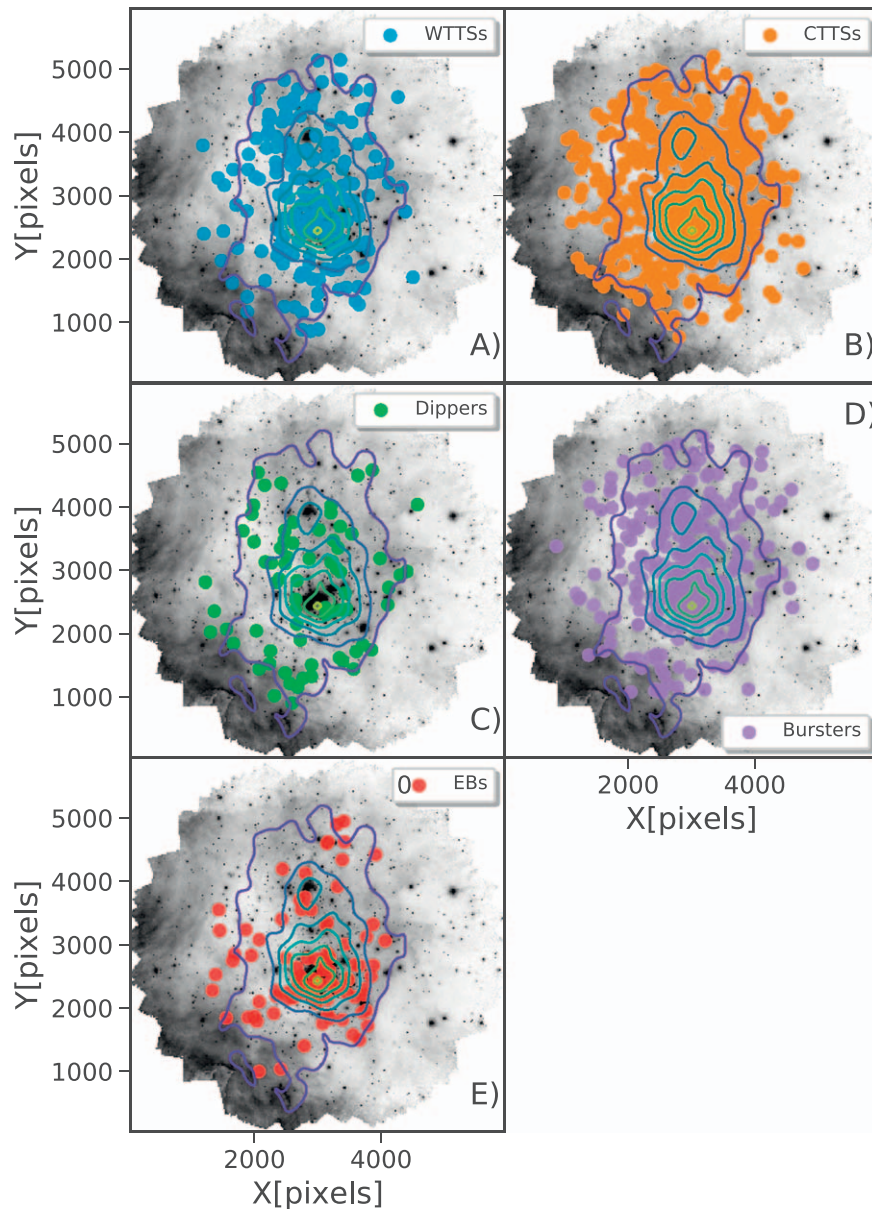


Figure 13. Spatial distribution of Wd2 5 populations of variable stars superimposed on a black and white image of Wd2. Wd2 stellar isodensity contours are shown for reference. The populations are shown in five different panels following the same color-scheme used in Figure 7.

nearby bright OB stars (e.g., Haworth et al. 2017), can significantly affect disk growth and evolution.

Similarly the different behavior at different masses of the various types of variables can provide information on the life span and size of the circumstellar disks as a function of the mass of the star, although these trends will have to be further investigated to properly evaluate the effect of incompleteness.

6. Discussion and Conclusions

The analysis of the Galactic YMC Wd2 with the WFC3 on board *HST* showed that these systems are gold mines for studying the properties of variable PMS stars and investigate the evolution of their circumstellar disks as a function of mass and age. In fact at least one-third of the intermediate- and low-mass PMS stars in Wd2 are variable. Based on the characteristics of their LCs, we classified the variable PMS stars as WTTs candidates, CTTS candidates, dippers, and

bursters. In addition, 2% of the stars below $6M_{\odot}$ are eclipsing binaries, with orbital periods shorter than 80 days.

By comparing the ratio of variable stars with respect to the entire cluster population per bin of mass (Figure 15), we find that the fraction of both WTTs and CTTS candidates decreases as we move toward lower masses, and, in the case of WTTs candidates, we notice a clear change in slope below $\sim 0.9 M_{\odot}$. This drop in stellar counts is likely an artifact due to the fact that below $m_{F814W} \sim 22$ the LCs become too noisy to detect periodic signals. In fact the fraction of EBs also significantly decreases around this magnitude limit.

The bursters are the only group of variables to show a significantly different population ratio: their number remains almost constant between ~ 0.5 and $0.9 M_{\odot}$ with the respect of other stars of similar masses and then considerably decreases at higher masses, suggesting that either this is a phenomenon mainly associated to relatively low-mass stars, or that at higher masses the inner disks have been already significantly cleared

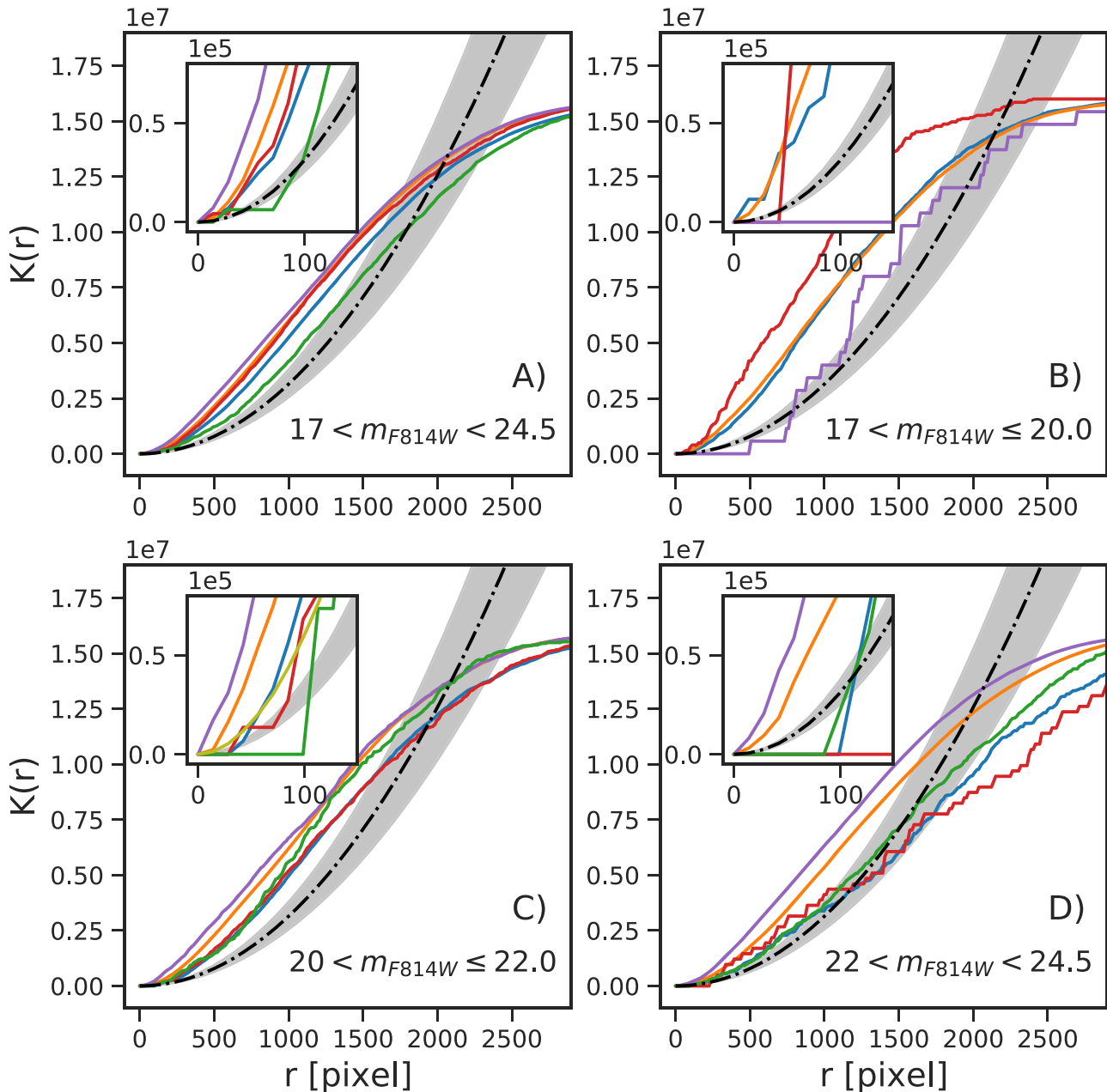


Figure 14. Clustering properties, as derived from Ripley’s K function, for the WTTS candidates (blue line), CTTS candidates (orange line), dippers (green line), bursters (purple line), and EBs (red line). The response of the K function for a Poisson distribution and the 90% confidence level are shown by the black dotted–dashed line and the shaded area, respectively. Panel (A) shows the clustering properties for all the variables fainter than $m_{F814W} > 17.0$ (corresponding to $\sim 3.3 M_{\odot}$ using Padova isochrones), panel (B) shows the behaviors of the stars between $17.0 < m_{F814W} \leq 20.0$ (which correspond to the mass range between ~ 1.75 and $3.3 M_{\odot}$, panel (C)) refers to the stars between $20.0 < m_{F814W} \leq 22.0$ (~ 0.7 and $1.8 M_{\odot}$), and panel (D) shows the properties of the fainter sources ($22.0 < m_{F814W} < 24.5$, corresponding to the mass range ~ 0.2 and $0.7 M_{\odot}$ using Padova isochrones).

and there is not enough material to feed strong bursts. In the latter cases Wd2 would provide us with a clock to estimate the evolution of the circumstellar disks as a function of stellar mass: while stars more massive than $\sim 1\text{--}2 M_{\odot}$ require less than ~ 1.5 Myr to considerably deplete their circumstellar disks, at lower masses the inner disks are likely more pristine, and can still provide a considerable amount of material to be accreted by the star.

The comparison among the spatial distributions of the five populations of variables highlights how local conditions can affect the evolution of circumstellar disks. In particular, dippers

appear to avoid the regions of higher stellar density, dominated by the high-mass stars. Over the years several authors have investigated how dynamical truncation (Vincke et al. 2015; Portegies Zwart 2016; Vincke & Pfalzner 2016), stellar winds (Pelupessy & Portegies Zwart 2012), dynamical interaction (Olczak et al. 2008; Reche et al. 2009; de Juan Ovelar et al. 2012), and photoevaporation from OB stars can affect the evolution of circumstellar disks. Recently, in simulating the effects of FUV radiation on circumstellar disks in clusters of different stellar densities, Concha-Ramírez et al. (2019) estimated that in regions of high stellar density about 80% of

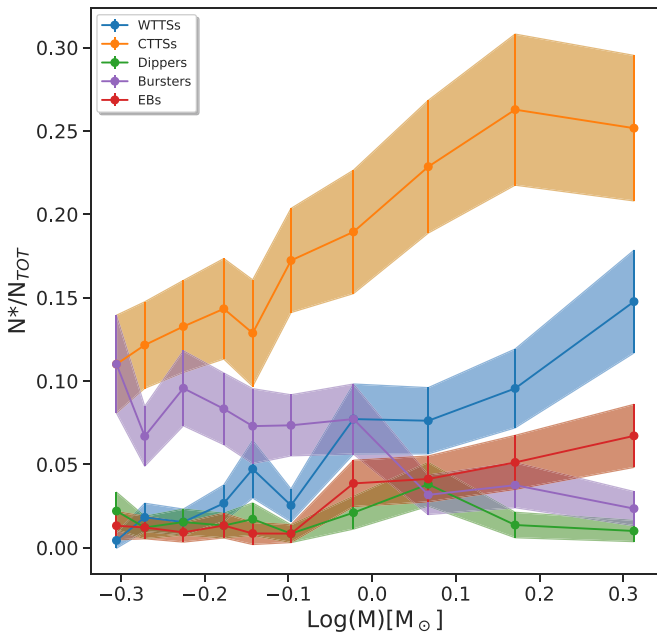


Figure 15. Ratio between the number of variable stars and the total number of stars in Wd2 per bin of mass between 0.5 and $2.4 M_{\odot}$. WTTs candidates are in blue, CTTS in orange, dippers in green, bursters in purple, and EBs in red.

the disks can be destroyed by external photoevaporation in less than 2 Myr while, in comparison, mass loss caused by dynamical encounters is negligible.

If the dramatic drop in luminosity experienced by the dippers is, as commonly accepted, due to the presence of large dusty structures and planetesimals, the absence of dippers in the two higher density clumps of Wd2 could explain why planetary systems appear to be extremely rare in globular clusters (Gilliland et al. 2000) and younger dense clusters (e.g., de Juan Ovelar et al. 2012). High spatial resolution follow-up observations in the near- and mid-infrared using, for example, NIRSpec and MIRI on the *James Webb Space Telescope* will be needed to definitely characterize the properties of the disks in Wd2 and other YMCs to determine how local conditions affect the evolution of these systems and the formation of planetary systems.

In future papers we will extend our analysis to the entire data set, and to the short exposures. With a better temporal sampling of the LCs, we will statistically estimate the duty cycles of the bursting episodes and better characterize the properties of the five populations of variable PMS stars as a function of mass. At the same time our better temporal coverage will allow us to explore a larger range of orbital periods for the population of EBs. Artificial star tests will allow us to quantify the impact of selection biases at different masses. Finally we plan to use image subtraction and proper motion analysis to identify and characterize the properties of long period binaries as a function of their positions in the cluster, and to investigate how dynamics and stellar feedback affect their formation and evolution.

We are grateful to the anonymous referee for the careful review and useful suggestions, that helped improving this paper. We thank Stefano Casertano, Guido De Marchi, Nino Panagia, and Mark Krumolz for useful and constructive discussions. These observations are associated with program Nos. 14087, 15362, and 15514. Support for the program Nos.

14087, 15362, and 15514 was provided by NASA through a grant from the Space Telescope Science Institute. D.J.L. acknowledges support from the Spanish Government Ministerio de Ciencia, Innovación y Universidades through grants PGC-2018-091 3741-B-C22 and from the Canarian Agency for Research, Innovation and Information Society (ACIISI), of the Canary Islands Government, and the European Regional Development Fund (ERDF), under grant with reference ProID2017010115. This work is based on observations obtained with the NASA/ESA *Hubble Space Telescope*, at the Space Telescope Science Institute, which is operated by the Association of Universities for Research in Astronomy, Inc., under NASA contract NAS 5-26555.

Facilities: *HST*(WFC3)—*Hubble Space Telescope* satellite, *HST*(ACS)—*Hubble Space Telescope* satellite.

ORCID iDs

E. Sabbi <https://orcid.org/0000-0003-2954-7643>
M. Gennaro <https://orcid.org/0000-0002-5581-2896>
N. Bastian <https://orcid.org/0000-0001-5679-4215>
K. C. Sahu <https://orcid.org/0000-0001-6008-1955>

References

- Alencar, S. H. P., Teixeira, P. S., Guimaraes, M. M., et al. 2010, *A&A*, **519**, A88
- Anderson, J., & King, I. R. 2006, Ins. Sci. Rep. ACS 2006-01 (Baltimore, MD: STScI)
- Ansdell, M., Gaidos, E., Williams, J. P., et al. 2016, *MNRAS*, **462**, L101
- Bell, K. R., & Lin, D. N. 1994, *ApJ*, **427**, 987
- Bély, P. Y., Hasan, H., & Miebac, M. 1993, Orbital variations in the Hubble Space Telescope, Instrum. Sci. Rep. SESD-93-16 (Baltimore, MD: STScI)
- Bodman, E. H. L., Quillen, A. C., Ansdell, M., et al. 2017, *MNRAS*, **470**, 202
- Bonanos, A. Z., Stanek, K. Z., Udalski, A., et al. 2004, *ApJL*, **611**, L33
- Bouvier, J., Cabrit, S., Fernandez, M., et al. 1993, *A&A*, **272**, 176
- Bouvier, J., Chelli, A., Allain, S., et al. 1999, *A&A*, **349**, 619
- Bouvier, J. P., Grankin, K. N., Alencar, S. H. P., et al. 2003, *A&A*, **409**, 169
- Cieza, L. A., Casassus, S., Tobin, J., et al. 2016, *Natur*, **535**, 258
- Clarke, C. J., & Bouvier, J. 2000, *MNRAS*, **319**, 457
- Cody, A. M., & Hillenbrand, L. A. 2018, *AJ*, **156**, 71
- Cody, A. M., Stauffer, J., Baglin, A., et al. 2014, *AJ*, **147**, 82
- Cody, A. M., Stauffer, J. R., Rebull, L. M., et al. 2017, in ASP Conf. Ser. 512, *Astronomical Data Analysis Software and Systems XXV*, ed. N. P. F. Lorente, K. Shorridge, & R. Wayth (San Francisco, CA: ASP), 13
- Concha-Ramírez, F., Wilhelm, M. J. C., Portegies Zwart, S., et al. 2019, *MNRAS*, **490**, 5678
- D’Angelo, C., & Spruit, H. C. 2010, *MNRAS*, **406**, 1208
- de Juan Ovelar, M., Kruijssen, J. M. D., Bressert, E., et al. 2012, *A&A*, **546**, L1
- De Marchi, G., Panagia, N., & Romaniello, M. 2010, *ApJ*, **715**, 1
- Gilliland, R. L., Brown, T. M., Guhathakurta, P., et al. 2000, *ApJL*, **545**, L51
- Green, J. D., Hartmann, L., Calvet, N., et al. 2006, *ApJ*, **648**, 1099
- Hartmann, L., Calvet, N., Gullbring, E., & D’Alessio, P. 1998, *ApJ*, **495**, 385
- Hartmann, L., Kenyon, S., & Hartigan, P. 1993, in *Protostars and Planets III*, ed. E. H. Levy & J. I. Lunine (Tucson, AZ: Univ. Arizona Press), 497
- Hartmann, L., & Kenyon, S. J. 1996, *ARA&A*, **34**, 207
- Hartmann, L., & Stauffer, J. R. 1989, *AJ*, **97**, 873
- Haworth, T. J., Facchini, S., Clarke, C. J., & Cleeves, L. I. 2017, *MNRAS*, **468**, L108
- Hedges, C., Hodgkin, S., & Kennedy, G. 2018, *MNRAS*, **476**, 2968
- Herbig, G. H. 2007, *AJ*, **133**, 2679
- Herbst, W., Bailer-Jones, C. A. L., Mundt, R., et al. 2002, *A&A*, **396**, 513
- Herbst, W., Herbst, D. K., Grossman, E. J., & Weinstein, D. 1994, *AJ*, **108**, 1906
- Hillenbrand, L. A., Herbst, W., Attridge, J., et al. 2002, arXiv:astro-ph/0210520
- Joy, A. H. 1945, *ApJ*, **102**, 168
- Kim, D.-W., Protopapas, P., Bailer-Jones, C. A. L., et al. 2014, *A&A*, **566**, A43
- Lallo, M. D., Makidon, R. B., Casertano, S., & Krist, J. E. 2006, *Proc. SPIE*, **6270**, 62701N
- Lata, S., Pandey, A. K., Chen, W. P., et al. 2012, *MNRAS*, **427**, 1449

- Lata, S., Pandey, A. K., Yadav, R. K., et al. 2019, *AJ*, 158, 68
- Lindegren, L., Hernández, J., Bombrum, A., et al. 2018, *A&A*, 616, A2
- Lomb, N. R. 1976, *Ap&SS*, 39, 447
- Marigo, P., Girardi, L., Bressan, A., et al. 2017, *ApJ*, 835, 77
- Marilli, E., Frasca, A., Covino, E., et al. 2007, *A&A*, 463, 1081
- McGinnis, P. T., Alencar, S. H. P., Guimarães, M. M., et al. 2015, *A&A*, 577, A11
- Moffat, A. F. J., Shara, M. M., & Potter, M. 1991, *AJ*, 102, 642
- Morales-Calderón, M., Stauffer, J. R., Hillenbrand, L. A., et al. 2011, *ApJ*, 733, 50
- Olczak, C., Pfalzner, S., & Eckart, A. 2008, *A&A*, 488, 191
- Pastorelli, G., Marigo, P., Girardi, L., et al. 2019, *MNRAS*, 485, 5666
- Pelupessy, F. I., & Portegies Zwart, S. 2012, *MNRAS*, 420, 1503
- Portegies Zwart, S. F. 2016, *MNRAS*, 457, 313
- Quanz, S. P., Henning, Th., Bouwman, J., et al. 2007, *ApJ*, 668, 359
- Raghavan, D., McAlister, H. A., Henry, T. J., et al. 2010, *ApJS*, 190, 1
- Reche, R., Beust, H., & Augereau, J.-C. 2009, *A&A*, 493, 661
- Rice, T. S., Reipurth, B., Wolk, S. J., et al. 2015, *AJ*, 150, 132
- Richards, J. W., Starr, D. L., Butler, N. R., et al. 2011, *ApJ*, 733, 10
- Ripley, B. D. 1977, *J. R. Stat. Soc. B*, 39, 172
- Ripley, B. D. 1979, *J. R. Stat. Soc. B*, 41, 368
- Rousseeuw, P. J., & Croux, C. 1993, *J. Am. Stat. Assoc.*, 88, 1273
- Sabbi, E., Anderson, J., Lennon, D. J., et al. 2013, *AJ*, 146, 53
- Sabbi, E., Lennon, D. J., Anderson, J., et al. 2016, *ApJS*, 222, 11
- Scargle, J. D. 1982, *ApJ*, 263, 835
- Sokolovsky, K. V., Gavras, P., Karamelas, A., et al. 2017, *MNRAS*, 464, 274
- Stassun, K. G., Mathieu, R. D., Mazeh, T., & Vrba, F. J. 1999, *AJ*, 117, 2941
- Stassun, K. G., van den Berg, M., & Feigelson, E. 2007, *ApJ*, 660, 704
- Vargas Álvarez, C. A., Kobulnicky, H. A., Bradley, D. R., et al. 2013, *AJ*, 145, 125
- Venuti, L., Bouvier, J., Cosy, A. M., et al. 2017, *A&A*, 599, A23
- Vincke, K., Breslau, A., & Pfalzner, S. 2015, *A&A*, 577, A115
- Vincke, K., & Pfalzner, S. 2016, *ApJ*, 828, 48
- Westerlund, B. 1961, *ArA*, 2, 419
- Xing, L. F., Shi, J. R., & Wei, J. Y. 2006, *NewA*, 12, 265
- Zeidler, P., Grebel, E., Nota, A., et al. 2016, *AJ*, 152, 84
- Zeidler, P., Nota, A., Grebel, E. K., et al. 2017, *AJ*, 152, 84
- Zeidler, P., Sabbi, E., Nota, A., et al. 2015, *AJ*, 150, 78
- Zhang, M., Bakos, G. A., Penev, K., et al. 2016, *PASP*, 128, 035001
- Zhu, Z., Hartmann, L., & Gammie, C. 2009, *ApJ*, 694, 1045